

## **Promoting convergence: the Phi spiral in abduction of mouse corneal behaviors**

Jerry Rhee<sup>1\*</sup>, Talisa Mohammad Nejad<sup>2</sup>, Olivier Comets<sup>3</sup>, Sean Flannery<sup>1</sup>, Emine Begum Gulsoy<sup>3</sup>, Philip Iannaccone<sup>1</sup> and Craig Foster<sup>2</sup>

*<sup>1</sup>Lurie Children's Research Center, Developmental Biology Program and Department of Pediatrics, Feinberg School of Medicine, Northwestern University, Chicago, IL, <sup>2</sup>Department of Civil and Materials Engineering, University of Illinois at Chicago, Chicago, IL, <sup>3</sup>Department of Materials Science and Engineering, Northwestern University, Chicago, IL*

## Abstract

Why do mouse corneal epithelial cells display spiraling patterns? We want to provide an explanation for this phenomenon by applying an idealized problem solving process. Specifically, we applied complementary line-fitting methods to measure transgenic epithelial reporter expression arrangements displayed on three mature, live enucleated globes to clarify the problem. Two prominent logarithmic curves were discovered, one of which displayed the  $\phi$  ratio, an indicator of the optimal configuration in phyllotactic systems. We then utilized two different computational approaches to expose our current understanding of the behavior. In one procedure, which involved an isotropic mechanics-based finite element method, we successfully produced logarithmic spiral curves of maximum shear strain based pathlines but computed dimensions displayed pitch angles of  $35^\circ$  ( $\phi$  spiral is  $\sim 17^\circ$ ), which was altered when we fitted the model with published measurements of coarse collagen orientations. We then used model-based reasoning in context of Peircean abduction to select a working hypothesis. Our work serves as a concise example of applying a scientific habit of mind and illustrates nuances of executing a common method to doing integrative science.

## Introduction

Convergence science<sup>1</sup> is a directed effort to take advantage of collective modern expertise to solve hard problems of organized complexity<sup>2</sup>. The goals and missions are expanded from a New Biology<sup>3</sup>, which stressed the coordinated application and education of problem-solving methods, employed by complements of experts with both deep and wide knowledge, to control and preserve the nested hierarchies that characterize healthy natural living systems. Despite the promise of merging disciplines<sup>4</sup>, it is recognized that an optimal level of interaction has not yet been achieved<sup>5-7</sup>.

The scientific habit of mind is a normative attitude toward learning and acting shared by both experts and novices<sup>8-11</sup>(CP 1.44). The associated property of simplification serves as antidote<sup>12,13</sup>(CP 7.61-73) for the growing sea of information that obstructs integration across disciplines. Despite potential benefits to society, effective dissemination and acceptance of the things that need to be communicated about the scientific method<sup>2,11</sup> in a concise, accepted form has proved extremely difficult<sup>14,15</sup>(CP 7.49). One goal of this report is to exemplify<sup>16</sup> an idealized approach<sup>17</sup> through application of modern techniques to solve an unexplained biological phenomenon. Extensive discussion is intended to emphasize particular themes, such as clarifying joint problem spaces<sup>7,18,19</sup> that promote effective collaboration. Stated differently, we want to explain why mouse corneal epithelial cells are arranged as spirals through application of a scientific habit of mind.

Why-questions about natural phenomena are in part searches for explanations, and providing accounts is a fundamental aim of science<sup>20</sup>. Sufficient explanations are three-term relations between a topic, a contrast-class, and a relevance relation, which “specifies what sort of thing is being requested as answer” for a given context<sup>21</sup>. Explanations to why-questions are never disinterested and can be structured into a logical form<sup>22</sup> using the Peircean abduction (PA), an adaptive syllogistic argument that leads to selection of the working hypothesis under uncertainty<sup>23</sup>. The PA differs from other statements of abduction (*cf.*, <sup>24</sup>) in that it draws special attention to the important role cognitive processes play in organizing and advancing scientific theories. That is, it guides transformation of our attitudes toward mental models<sup>25</sup> from surprise (other than expected) -> suspect (relevance relation) -> matter of course (belief/habit). It states:

The surprising fact, C, is observed.  
But if A were true, C would be a matter of course.  
Hence, there is reason to suspect that A is true. (CP 5.189)

Therefore, the extent to which a mechanism (A) qualifies as a working hypothesis for explaining observation (C) depends on judgments about how much deductions of (A) suffices expectations for (C).

Spirals can be used to distinguish different forms of nature and at different growth stages<sup>26-28</sup>. Natural planar spirals are typically classified as either Archimedean or logarithmic depending on rate of growth of radiating arms. The

$\phi$  spiral is a special type of a logarithmic spiral in which the radius grows proportionally to the  $\phi$  ratio (1.618...) and can be described by its pitch angle of  $\sim 17^\circ$ . A pitch angle is defined as the angle formed at the point where the tangent of the spiral arm meets a circle (inset Fig3a).  $\phi$  is an irrational number approached by the quotient of the greater number to its previous term at the limit of the Fibonacci series. This number can also be derived by dividing a line/circle the only way allowable, such that taking the ratio of the larger to the smaller equals the proportion of the whole to the larger of the two pieces<sup>29</sup>.

Spirals have been decomposed and computed in natural systems across vast spatial scales<sup>30-33</sup>, which provide opportunities for synthesizing sound relations across disciplines<sup>34</sup> through structural alignment<sup>35</sup>. Therefore, the practice of explaining why spirals occur in mouse corneas may be exapted for different purposes, such as improving biomaterials design<sup>36,37</sup>, maintaining health<sup>38-41</sup> or clarifying general constraints among locally planar, globally spherical systems<sup>42,43</sup>.

Spirals have been reported on the anterior surface of human eyes under both normal and aberrant conditions. Vortex keratopathies are recognized by metabolic or drug depositions on the anterior surface while hurricane keratopathies are classified as diseased or natural forms associated with epithelial cell behaviors<sup>44</sup>. The stability of some corneal spirals are illustrated by longitudinal analyses, which showed that subtle changes to neural plexus arrangements can be detected over weeks-long timescales<sup>45</sup>. An *in vitro* study of corneal limbal explants exposed to a specific magnetic field produced spirals that maintained up to  $\sim 1$ wk before unfurling<sup>46</sup>.

In the rodent, spirals are prominently displayed as *transgenic epithelial cell segregation arrangements*<sup>47,48</sup> or as neural extensions<sup>49-51</sup> migrating through the subbasal nerve plexus<sup>52</sup>. Mosaic studies<sup>47,53</sup> showed that spirals of reporter expression arrangements begin to emerge  $\sim 3$ weeks after birth ( $\sim 1$ wk after eye opening) and resolve to robust patterns after  $\sim 10$ wks, a time that marks the later part of sigmoidal growth<sup>51,54</sup>. These observations of spiral patterning in distinct layers of the cornea is suggestive of a global systemic force that regulates formation and maintenance<sup>55</sup>. Despite proposal of a contrast class of mechanisms (*e.g.*, electrical, magnetic, mechanical, cellular<sup>44,56-59</sup>), there is currently no consensus on a best explanation.

In this report, we surveyed live, enucleated globes from transgenic mouse corneas between 4 and 7 months using confocal laser scanning microscopy. We applied complementary line-fitting measurements to demonstrate that  $17^\circ$  and  $21^\circ$  pitch angles are predominantly represented. We constructed two different computable schemas to simulate observed behaviors. Subsequently, we combined abduction and model-based reasoning to make inferences about deduced solutions, which reflect our current understanding of the phenomenon. We close with a discussion of justifications for choosing the working hypothesis (CP 7.163).

## Results

### *Mouse Cornea Anatomy*

The cornea is the superficial, transparent, avascular tissue at the anterior-most position of the eye (Figure 1). It may be considered a special type of skin<sup>60-62</sup> with balanced optical and mechanical properties that may be exploited for development and application of therapeutic technologies<sup>63-65</sup>. Structurally, it is a three-layered system (Fig 1d, j-l) with the stratified corneal epithelial cells further subdivided into superficial cells (white arrows, Fig 1d,e), intermediate wing cells and basal epithelial cells (red arrows, Fig 1d,f,j). The different cell types are marked by layer-specific expression of different proteins, such as the tight junction marker, ZO-1 (Fig 1e) only in superficial cells, while basal epithelial cells predominantly express the gap junction protein, Cx43 (Fig1f and inset) and Integrin  $\beta 4$ , a mechanical/signaling integrator, but with local concentration differences (Fig 1f)<sup>66</sup>. The middle layer of the cornea, the stroma (Fig 1d,k), is comprised mostly of a collagen-rich material secreted by keratocytes<sup>67</sup> (green arrows, Fig 1d,j,k), the path-dependent arrangements and interactions of which provide the majority of mechanical support. The deep corneal endothelial cells (purple arrows, Fig 1d,l), arranged in shapes reminiscent of the Benard phenomenon<sup>68</sup>, provide important fluid regulation required to maintain transparency and general nutritive balance<sup>69,70</sup>.

The limbus (light blue arrows, Fig 1a-c,g-i), a morphologically distinct region that also serves as a specialized niche for stem cells<sup>71</sup>, marks the corneal periphery. The stroma is split immediately posterior to the limbus, with the superficial portion providing basal support to the conjunctiva, a goblet cell-rich layer contiguous with the cornea that provides mucus and protection against foreign substances in combination with the lacrimal apparatus. The sclera constitutes the exterior portion of the posterior eye.

#### *Qualitative determination of spiral progression through comparisons*

Previously, we used a landmarking method to demonstrate that logarithmic spiral patterns are conserved in chimeric rat corneas<sup>48</sup>. In the current report, we used a line-fitting method to measure variegated arrangements displayed by *mTmG* alleles<sup>72</sup>, *i.e.*, from individuals of a single genotype.

The *mTmG* transgenic line expresses a single-copy, membrane-targeted version of a fusion reporter gene homologously recombined into the *ROSA26* locus, supplemented by a strong artificial promoter to enhance activation. Although expression was expected in every cell, only mosaic patterns were observed in adult mouse corneal epithelia. We observed different types of patch patterns using the same artificial promoter expressing a different downstream reporter integrated randomly into the genome<sup>73</sup> (data not shown). Variegation in *Krt12-Cre/+; ZEG* reporter mice have also been reported<sup>74</sup>. In rats, transgenic lines produced by lentiviral injection of a reporter construct driven by a human polyubiquitin-C promoter that express a more complete pattern has been reported<sup>48</sup>. The reasons for corneal-specific variegated patterns is a subject of future investigations but is expected to involve combinations of epigenetic<sup>75,76</sup>, physiological<sup>77</sup> and/or dynamic protein turnover mechanisms. Therefore, whether spiral patterns represent clonal cell migration paths or transient reporter effects are not known, although the

former has generally been assumed in the absence of complete information.

To determine regularity of *mTmG* variegated patterns, we examined a developmental cross section of enucleated live mouse corneas from 4 to 7 months, taking great care not to perturb the natural shape of the globe. Comparisons of globes from different individuals arranged in series suggested that spirals evolve over time but ordering does not behave monotonically (Fig 2a-c). When intra-individual corneas were compared, similar or topologically non-equivalent behaviors were displayed on surfaces of paired eyes. For example, in one 6month old female, clockwise (CW) spirals were displayed on each cornea (Fig2d,e), whereas a different individual displayed a counterclockwise (CCW) pattern on one eye but two counter-rotating curves separated by an equator on the other (Fig2f,g). In mice, CW spiral patterns dominate ~5% over CCW patterns but these patterns only represent a subset of possible forms<sup>47</sup>. Probability distributions of main pattern types are characterized in<sup>53</sup> based on examinations of 135 globes. Combined, these observations demonstrate that both genetic and environmental effects influence mature patterns, which may depend on unequal spontaneous symmetry breaking processes operating at earlier sensitive periods<sup>78,79</sup>.

### *Visual search for spirals*

To demonstrate the existence of logarithmic spirals on mouse corneas and to determine their precise pitch angle, we matched pre-selected curves to features. Due to incomplete information about features, we used reasonable grouping principles<sup>80</sup> (*viz.*, proximity, similarity, continuity, smooth continuation, symmetry, familiarity and common fate) for categorization. Only corneas from age-matched animals with qualitatively similar shapes were selected for measurement to focus our problem to a discrete growth stage.

We produced a range of curves for direct comparisons. The range was selected based on resemblance to natural forms; the 12.44° pitch angle representing the silver ratio displayed by nautilus<sup>81</sup>, the  $\phi$  ratio displayed in Phyllotaxis<sup>82</sup>, the 21.1° pitch displayed by the M51 Galaxy<sup>83</sup>, as well as extreme forms, which are together represented in Fig3.

We first performed a blinded study to mitigate subjective bias. Protocol for matching involves feature selection/visual recognition of areas of contrast (arrows, Fig3a,b) followed by masking spiral arms through translation and/or rotation to generate the best fit. After a visually apparent feature is selected (purple arrow, Fig3a), a relationship to a second feature, such as the major curve (blue arrow) or distance to the pole (green dot) can be scanned and compared with each other. That is, the investigator is able to resolve distance to the center<sup>84</sup> to micrometer resolution by taking advantage of subordination of coiling forms<sup>85</sup>, *viz.*, the relationship between the pole and radiating arms<sup>26</sup>. Selection of two features also constrains rotational freedom, which drastically reduces the space to be examined for correlations (purple and orange arrows). That is, the protocol makes the difficult problem of describing the full extent of the complex pattern displayed on mouse corneas tractable by reducing the problem to measurements of localized,

selected regions. Comparison to a counterexample demonstrates that the visually apparent argument for a better match is self-evidencing (Fig3b,c).

Best fit was determined through direct contrast against overlain curves of similar angles (Fig3d,e). An external viewer is then able to verify the investigator's intention through assessment of the precise relationship between crossing point and selected feature at the bound site (purple arrow, Fig3e). Intuitive preliminary matching at the intended site (purple arrow, Fig3d) yielded imprecise crossings, which can be refined through deliberate recursion onto a selected representation (Fig3e,<sup>13,86</sup>).

In the absence of explicit knowledge about underlying mechanisms of cell variegation, judgment<sup>87</sup> was used to determine best fit. For example, if the conspicuous major arm was deemed most important, the 21.1° spiral was the best match (Fig3g,h). However, this came at a cost of losing match with the edge marked by the purple arrow (Fig3g,h) that extended to a bending feature at a distal site (yellow arrow, Fig3i). If all features are commensurable, then the  $\phi$  spiral was the best match because it touched the greatest number of features along the greatest distance from the pole.

Once selected, targeted search<sup>88</sup> for periodic effects can be implemented by rotating the selected curve at desired increments (five-fold rotation, green arrow, Fig3f), which suggests discrete parsing of territories. Rotating measuring sticks 180° after matching to the major arm always produced overlap with features of the minor arm in *this* sample (range: 8° to 35°, orange arrows, Fig3g,h). These measurements suggest the existence of opposite symmetrical logarithmic spiral arms in *this* cornea. In summary, placement of each curve onto a scene produces a hypothesis about non-random effects being responsible for generation of that correlation.

#### *Verification for existence of $\phi$ and M51 spirals*

To support the validity of our method and to minimize influence of illusory effects, we transformed the images from Cartesian to log-polar coordinates (Fig4). Each pixel is then referenced by the logarithm of its distance to the pole and the angle between that line and the x-axis. With this method, any logarithmic curve is converted into an oblique line, the slope of which is related to the pitch angle. For some of the data, we performed log transformations using different poles (Fig 4b-c, d-e) and visually inspected the data for presence of straight lines. Display of degree angle is sensitive to pole selection and subsequent confirmation through visual perception is affected by feature transformation.

We primarily chose visually apparent features, such as clusters of bright cells lying in sequence (yellow arrows, Fig4b) or edges to determine linearity. The reader can then assess correspondence of matched features or verify existence of parallel lines in adjacent regions (orange arrows Fig4).

We emphasize that while the  $\phi$  spiral was noticed, it was *not* the most conspicuous form displayed in the three samples using this method. Rather, the 21.1° angle was. Moreover, while the entire set of possible logarithmic curves is not currently known, the range was found to be discontinuous. For example, although

the 21° curve was dominant (white lines, Fig4f-j), more extreme pitch angles (green arrows, Fig4c,d) were also represented.

#### *Measuring size of core*

If radiating arms are measureable, then so should centers of curves. Briefly, three spiral corneal samples were normalized by drawing a line across a linear feature (white lines, Fig5), rotating five times, then matching to generate the outlines of a pentagram (Fig5a,d). Samples were oriented by subjectively rotating the image with respect to the top horizontal line (Fig5a,c, purple arrows). Adjusting samples proved useful for partitioning the space for easier comparison and representation (Fig5, a-d). That is, it fixed searchable space to a smaller region by restricting free rotation that facilitated representation of pole distributions.

Using this method, we identified poles for each image based on matching distal-arm features (Fig5d). Curve-fitted poles from each rotated sample were then compiled onto single images (colored dots, Fig5b,c). We defined the size of the core as the maximum distance of the two most separated poles. The results from images captured with a 10X lens were 50µm, 145µm and 210 µm, respectively (Fig5a-c). Projecting 3D curved samples onto a 2D plane is expected to increase measurement error in samples collected at lower magnification. These data argue that curves are not always tiled on a plane. That is, although the poles in the first sample pivoted about a single point when examined at higher magnification (Fig. 3f), the arms of samples with larger cores crossed each other near the center.

#### *Deducing solutions from one model*

One model of corneal epithelial patterning proposes that spirals result from preferential placement of stem cells at the limbus followed by migration of differentiating cells toward the pole<sup>53,54</sup>. To illustrate the chemotactic mechanism as a potential explanation with respect to the three-term relation, we produced a multi-agent model using Netlogo software. The multi-agent modeling platform allows constructions of appropriate problem representations by facilitating conversion of mental models<sup>25</sup> into computer simulations<sup>89</sup>. For our purposes, we integrated rules for firefly flashing and *Dictyostelium* aggregation behaviors.

Briefly, stem cells (large dark blue discs, Fig6a) placed at the limbus (light blue annulus) produce epithelial cells (agents, maple leaves). Agents move in response to two different parameters. The first value is assigned to patches (static positions represented as yellow surface) that is highest at the pole. The second value is dynamic; a diffusing chemical secreted by agents, to which neighbors respond with an assigned probability. Chemical concentrations can be assessed through visual inspection of signal intensity (bright green, Fig6b). The rules allow up to 10 cells to occupy the same discrete space to produce a dynamically stable number of cells. Global arrangement can be approximated using a box-counting algorithm that is exported to calculate fractal dimension  $D$  (Fig6c,i). These rules are sufficient to satisfy the conditions of the stem-cell based model proposed to explain epithelial spiraling, although stem cell positions are fixed<sup>53</sup>.



Simulations allow views of time slices during the ontogenetic process. Export views at  $t=0$  or  $t=400$  iterations are presented to give the reader an idea of the effects of parameter selection on final solutions (Fig6d-g). Export views from a single simulation with Sniff angle 45 are presented in series in Fig6h. "Sniff angle" is a simulation parameter that allows agents to select detection range in direction of heading that affects direction of the next movement.  $D$  is plotted for increments up to 800 iterations under different conditions ( $\sim 80$  days, based on rate of spiral emergence, and speed of migration, measured at  $\sim 26\mu\text{m}/\text{day}^{54}$ ). Based on both direct visualization and plot, dynamic equilibrium was achieved after  $\sim 400$  iterations. Comparisons of different initial conditions demonstrated that the most constrained global shape resulted from sniff-angle 68 degrees and addition of pacemakers. Parameters can be adjusted to yield different forms, including a spiral (Fig 6j), target (Fig6k) or saddles (Fig 6l).

#### *Induction through comparison against target behavior*

Comparison of the hypothesized global representation of observed behavior against computed solutions quickly exposed the ambiguous meaning of the term "spiral" (Fig6j). For example, juxtaposed breaks that contribute to the sense of spirality are positioned at the periphery, whereas in natural corneas, peripheral patterns are radial and break into spirals  $\sim 300\mu\text{m}$  from the pole (Fig3i). To our knowledge, epithelial assortment patterns that resemble targets have never been observed on natural corneas, which suggest that real conditions do not allow for its formation and maintenance. Although counter-rotating pairs have been observed in simulations, its shape is different and positioning is outside the domain in which it is normally found (field size = 3mm, each parallel segment in this image is  $\sim 70\mu\text{m}$ , central domain radius = 3 segments, closest saddle point is 4 segments from pole).

Although our agent-based model can be criticized for many deficiencies, such as individuated migration rather than contact-mediated coordination, failure to cover the expanse of the migrating field, large migration step sizes, *etc.*, it is nevertheless useful for exposing unstated assumptions that require explanation, *viz.*, its location at the center of the cornea and the specific pitch angle. Moreover, it is not clear that even a perfectly executed chemotactic model would produce the desired logarithmic spiral solution since primary forms in *Dictyostelium* models resemble Archimedean spirals. That is, computed solutions did not appear to reduce the number of possibilities, as no clear relevance relation was recognized.

#### *Deducing and comparing solutions from a different model vs. target behavior*

To produce a contrast class, we constructed a bulk material model with either isotropic stiffness or one that adds anisotropy through collagen alignments matched to reported experimental measurements<sup>90</sup> (Fig7a). Under stated constraints, displacement is greatest at the center when a pressure of 13mm Hg is applied to the interior surface (Fig7b). From this solution, we mapped a vector field of maximum shear strains in the plane of the surface of the stroma (Fig7c). To simplify visualization, we devised an algorithm that traced pathlines from the perimeter based on sampling local maximum shear strains using an unstructured

mesh under isotropic conditions (black curves, Fig7d, center region magnified below and collated as black curves in Fig7f). When a radial mesh was applied to isotropic conditions, pathlines resolved more closely to  $35^\circ$  pitch angles (green curves, Fig7d;  $35^\circ$  red curve overlaid to illustrate precision of measurement, Fig7d). Comparison of black and green curves demonstrates local differences that illustrate sampling effects but global behaviors are relatively unaffected.

To test the hypothesis that simulated collagen arrangements can affect pathline behaviors, we repeated procedures under anisotropic conditions using the radial mesh (blue curves, Fig7e,f). We directly compared pathlines initialized from five independent positions under the three conditions, *ie.*, black, green and blue curves. When anisotropic collagen conditions were applied, shapes of curves were qualitatively different at the center (Fig7f). Curves that were both greater (purple arrow, Fig7e) and lesser (orange arrow, Fig7e) than a  $35^\circ$  logarithmic curve were observed under anisotropic conditions using a radial mesh.

In summary,  $35^\circ$  logarithmic maximal in-plane spiral shear pathlines were produced under isotropic conditions that differed from the  $\phi$  spiral by  $18^\circ$ . Adding collagen anisotropies affected shape of solutions maximally near the center. These data support the argument that local anisotropies of collagen arrangements can affect pathline behavior. Moreover, we hypothesize that if collagen arrangements are major effectors of patterns displayed on mouse corneal epithelial cells, then actual arrangements, which are known to be more complex than the coarse forms that we used to fit our model, can lead to  $\phi$  spiral shear strains. Our approach offers a complementary method by which to solve mesoscopic collagen arrangements<sup>91</sup>.

## Discussion

Being clear about the relation<sup>21</sup> (CP 5.189) between behaviors to be explained<sup>92,93</sup> and mechanisms of formation<sup>37,94-96</sup> is an under-appreciated requirement for productively advancing transdisciplinary investigations of scientific explanation, which ultimately bears on practical judgment making<sup>87</sup>. We applied complementary line-fitting methods to verify existence of two prominent logarithmic spiral forms. Despite resolvability of the measuring method, we were not able to agree on a single value to describe the global state of the system. Specifically, the nondiscursive nature of the matching method (Fig3d) and the lack of awareness of underlying biology both affected feature appraisal, which affected consensus building. However, if future investigations<sup>7,87</sup> (CP 7.114-115) reveal grounds for assigning higher value to the conspicuous feature (blue arrows, Fig3), then the best description would be  $21^\circ$  (Fig3g). If all features are commensurable, then the  $\phi$  spiral is the best representation because a single curve touches the most number of landmarks along the greatest distance from the pole (yellow arrow, Fig3i). Irrespective of such considerations, the resolution of the measuring method was resolvable at least to within  $4^\circ$ , and makes description of the end flexible but not ambiguous<sup>87</sup>.

To avoid vacillation<sup>97</sup>, we hypothesized that the  $\phi$  spiral is the global attractor<sup>34,82</sup>, or a type of regulating line that saves the phenomenon. It was

preferred over the  $21^\circ$  spiral based on its utility as a computable descriptor for minimal energy/maximum entropy/perfect growth<sup>28,32,98</sup> states.

Qualitative matching of the  $\phi$  spiral against solutions to Netlogo simulations quickly exposed unstated expectations of the problem, *viz.*, explaining its location at the center of the cornea and whether the phenomenon can even be said to be present. Therefore, consonance between the Netlogo model and the observation is not produced the way the mechanism is currently posed.

To generate a computable contrast-class, we constructed an FEM model that produced logarithmic spiral shear strains under isotropic conditions. Upon simulation of intraocular pressure, curves displayed  $35^\circ$  pitch angles. Adding anisotropic collagen arrangements to the model impacted in-plane shear strain behaviors maximally near the center. Therefore, admissibility of the FEM model as a potential explanation depends on the likelihood that generation of a logarithmic curve is a veridical statement that the phenomenon is present and whether further modifications to the model reflecting finer measurements can affect tightening of curvature to  $17^\circ$ . That is, the choice of the working hypothesis ( $\phi$ , FEM model), in contrast to rest of contrast-class X (*i.e.*, Netlogo model), because A (deduction of logarithmic spiral, relevance relation)<sup>21</sup>. Adopting the hypothesis that the  $\phi$  spiral describes the global state of the system proved valuable for structuring the abduction, which then allowed simple performance evaluation via the relevance relation during induction, *sc.*, inference to the best explanation<sup>99</sup> (CP 7.218).

Corneal mechanical properties are scale dependent<sup>91</sup>. Collagen molecules self-organize into right-handed triple helical procollagen, are secreted by the generating cell, is processed enzymatically, associate laterally and longitudinally to produce collagen fibrils that are constrained in its properties by the microenvironment. Fibrils are  $\sim 30\text{-}35\text{nm}$  dense and  $\sim 1\text{mm}$  long<sup>100,101</sup> in the cornea. Fibrils then associate into larger lamellar forms  $\sim 2\mu\text{m}$  thick and  $\sim 5\text{-}100\mu\text{m}$  wide that interdigitate and insert directly into the Anterior Limiting Lamina<sup>102,103</sup>. Within lamella,  $\sim 50\text{-}60\text{nm}$  fibril spacing is maintained in a quasi-hexagonal arrangement by osmotic and electrostatic pressure mediated by proteoglycan coating of fibrils<sup>70</sup>. Fibril and lamellar sizes are controlled by region-specific, overlapping<sup>104</sup> and independent<sup>105</sup> mechanisms. Cholesteric forms detected with polarized microscopy<sup>37,102</sup> (Fig1k) implicate extracellular liquid crystalline packing as effectors of corneal mechanics<sup>106</sup>.

We experienced difficulty imaging the cornea at high resolution in whole organisms due to corneal pulsing. We suspect this is due to perfusion pressure driven from retinal and uveal vessels<sup>107</sup>. Given the rapid mouse heartbeat<sup>108,109</sup>, ocular pulsing may drive strain stiffening depending on the structure of interparticle interactions<sup>110</sup>.

Despite atomistic simulations of idealized microfibrils that neatly illustrate reliance of mechanical properties on the level of description<sup>91</sup>, the great disparity of observations reported in the large-strain regime demonstrates that mesoscale behaviors remain unexplained. Moreover, there is currently no systematic means by which to select samples that represent local corneal microenvironments appropriately enough to identify mesoscale-level regularities. If our hypothesis that

corneal spiral patterns are dependent on collagen arrangements is true, then the shape of the spiral, which situates the complex interactions that control its form<sup>111</sup>, will be useful for marking specific local microenvironments that can be developed into a reference system of reduced complexity<sup>7</sup>. That is, selection of a region that fits in a single optical field will help reduce experimental and computational costs of determining typicalities of mesoscopic arrangements, which can then complement studies concurrent with bottom-up methods<sup>91</sup>. Producing a comprehensible model that demonstrates quantitative dependence of the corneal spiral on molecular packing<sup>112</sup> will be an important and valuable contribution to understanding relationships between patterns and scaling phenomena<sup>113</sup>. Comparisons of behaviors using natural and engineered mice with defective organization<sup>38,40,114</sup> will support this mission to integrate diverse expertise to construct hypotheses that can also explain emergence of topologically non-equivalent forms (Fig 2g).

The mouse cornea shares similarity with plant phyllotaxis in that each can be considered a centric representation<sup>32,93,115</sup> of multi-layered pressure vessels displaying visually apparent spiral arrangements. Yet, the  $\phi$  ratio is expressed differently in the cornea, a transparent animal tissue in which growth and migration is towards the apex. Such properties make corneal spiraling incongruous with phyllotactic models in which the optimal process involves successive appearance of elements displaced at golden angles that grow away from the center, which secondarily produce spirals displaying the Fibonacci series.

To our knowledge, only an indirect phyllotactic mechanism has been applied for the cornea. Investigators have applied phyllotactic algorithms to compute tropocollagen packing into cylindrical fibrils that retain the property of placing elements on a generative spiral, which produce nearest neighbor-aligned parastichies<sup>116</sup>. Whether these nanoscale effects address our search for an explanation across the micrometer scale relevant for cell interactions<sup>91,103,117,118</sup> is unclear. In summary, while both systems are marked by the  $\phi$  ratio, the extent of common relational structure is ambiguous.

## Conclusions

The surprising fact, C ( $\phi$  spiral), is observed.

But if A (FEM model) were true, C would be a matter of course.

Hence, there is reason to suspect that A is true.

We produced the above working hypothesis by stating the topic, contrast-class and relevance relation<sup>21</sup> explicitly. The logarithmic spiral played different roles during the procedural stages of scientific explanation: 1) it served as a single numerical description for the observation, which rooted the abduction; 2) it served as the relevance relation by which to judge the quality of deductions from among the contrast class of models, which embodies the context<sup>25</sup> during inference to the best explanation. Our example serves as a concise example of scientific reasoning during early stages of inquiry and illustrates dependence of induction on abduction, and the serial manner by which different forms of hypothesis partition the process

(CP 7.218).

In summary, we propose that spiral angles are stable in mature mouse corneas (Fig8). They (co-) exist primarily as either 17° or 21° forms, the poles of which are superposed to different levels (Fig8d). We selected the combination of  $\phi$  spiral and FEM model as the working hypothesis based not only on resemblance of computed solutions to the observation, but also on integrative qualities such as contiguity, communicability and sustainability<sup>17,119</sup>.

## Materials and Methods

*Immunohistochemistry:* Standard immunohistochemical protocols were followed. The major modification added to the current method was to include an overnight 50nM Deoxycholate incubation in PBS at 42° prior to vibratome sectioning and incubation with primary antibody. Primary antibodies were purchased from BD Biosciences (Integrin  $\beta$ 1,  $\beta$ 4), ZO-1 and all secondaries from Invitrogen, Cx43 from Cell Signaling Technology and Laminin from Sigma.

*Live imaging of enucleated globes:* Animal work was approved by the Lurie Children's Research Center IACUC protocol 2009-09. Mice were euthanized according to IRB protocol. Globes were carefully removed using small scissors and placed in DMEM at room temperature. Corneas were placed in a culture dish with glass bottom and images were collected using an Olympus FV1000MPE with Spectra Physics MaiTai-OL HP ultrafast IR laser, and a BX61WI fixed stage upright microscope or using a Zeiss LSM 700. The SHG images were acquired at 860nm and filtered at 420-460nm bandpass filter in a reflected non-descanned PMT. Images were processed with Photoshop, conforming to epistemic standards for processing<sup>120</sup>.

*Netlogo model:* Coarse-grained algorithms borrowed from a library of validated models were modified to simulate conditions of corneal patterning. Example models used were Slime.nlogo and Firefly.nlogo. The model and details are freely available at the Center for Connected Learning at Northwestern.  
<http://ccl.northwestern.edu/netlogo/models/community/Cornea%20patch%20formation>

*Finite Element Method (FEM) model:*

Interior and exterior surfaces were fit to spheres of different radii and centers to create a central thickness of 0.3 mm and a peripheral thickness of 0.1 mm. The radius of the cornea is 1.4 mm. The geometry is then meshed with standard finite element meshing software using 8-node hexhedral elements with a B-bar option described in <sup>121</sup>. Both an unstructured mesh and a radial mesh with more elements near the center were used.

The material model is adapted from anisotropic, hyperelastic model for human corneas described in (104), but with a single preferred fibril orientation. We

model only the stroma. We treat the stroma as an isotropic, incompressible Neo-Hookean matrix, with a set of oriented and dispersed fibers that add stiffness in the direction in which they are oriented. Individual fibers are not modeled explicitly. The list of material properties are listed in Table 1.

**Table 1. Material properties for finite element model of the mouse cornea.**

$\lambda$ (kPa)	$\mu_0$ (kPa)	$k_1$ (kPa)	$k_2$
5500	60	20	400

We developed an approximate model for collagen orientations in the cornea based on the D28 data from Fig5 of (65). It is worth noting that while the collagen is predominately nasal-temporal near the center in the figure, the authors report other corneas exhibited a more oblique orientation near the center. Near the limbus, 90% of fibrils are assumed to be oriented circumferentially, while 80% are oriented horizontally near the center. Random fibril orientation, which makes up the difference, is not represented in the image. A transition zone bounded by the green and red circles linearly interpolates both the fibril direction and percentage of oriented fibrils. In this model, we use  $r_{in}$  of 0.5 mm and an  $r_{out}$  of 1.1 mm. The edge of the cornea is not allowed to displace but may rotate under pressure. An intraocular pressure of 13 mm Hg was applied to the inside face of the model.

The displacements, strains, and stresses are solved using a nonlinear finite element code. Since there are two orthogonal directions of maximum shear strain, we chose the one at each point that point counterclockwise (CCW) as it moves toward the center. We then traced pathlines of the vector field along the top surface. To simplify this procedure, we first averaged the shear strains in the element. Since the maximum shear strain direction is then constant within a given element, the trace of the pathline is piecewise linear. We then find the endpoint in each element, and trace the entire pathline, as described in <sup>122</sup>.

## Acknowledgements

We would like to thank Forrest Stonedahl for support with the Netlogo Model, Greg Taborn, Steve Iannaccone, Denise Lilly, Yolanda Palmer and Tim Skimina for administrative and computer support. We thank David Wokosin, Weiming Yu, Philip Hockberger, Satya Khuon, Teng-Leong Chew and James Lopez for microscope support. The research was supported by NIH 1R21EY020946-01 (JR, PMI, CF), NINDS NS054850 (subcontract, PMI) and the George M. Eisenberg Foundation for Charities (PMI).

## Figures and Legends

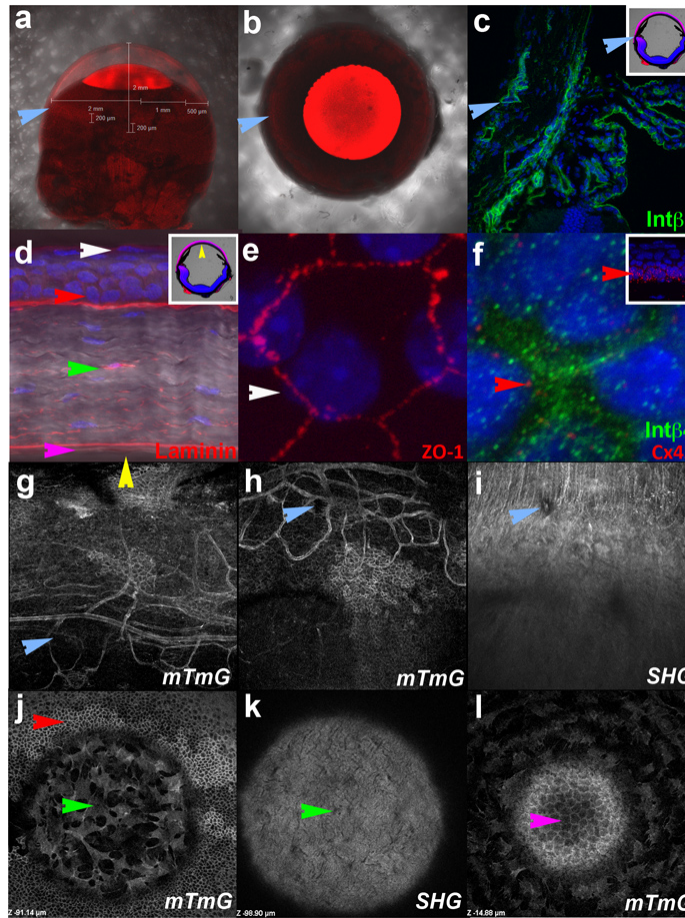


Fig1: Mouse cornea anatomy. a) Lateral and b) centric views of live, enucleated cornea. The red color is epifluorescence from the *mTmG* allele. c) Sagittal section of limbus infused immunostained using an Int $\beta$ 1 primary antibody to label some endothelial compartments. d) High magnification of region marked by the yellow arrow in inset. Basement membranes adjacent to Bowman's and Descemet's membranes are indirectly labeled with a Pan-Laminin antibody. e) Superficial cells (white arrows) are labeled by a tight junction marker,  $\alpha$ ZO-1. f) Int $\beta$ 4 and Cx43 antibodies mark puncta in basal epithelial cells, some of which are clustered in series. Live imaging of limbus using confocal (g,h) or polarization microscopy (i). Note loss of birefringence in sclera, indicating poor collagen alignment. Centric views of an optical plane through Bowman's membrane (j), stroma (k) or Descemet's membrane (l). Light blue arrows mark the same area of the limbus, white, red, green and purple arrows mark superficial cells, basal epithelial cells, keratocytes and corneal endothelial cells, respectively. SHG= Second Harmonic Generation.

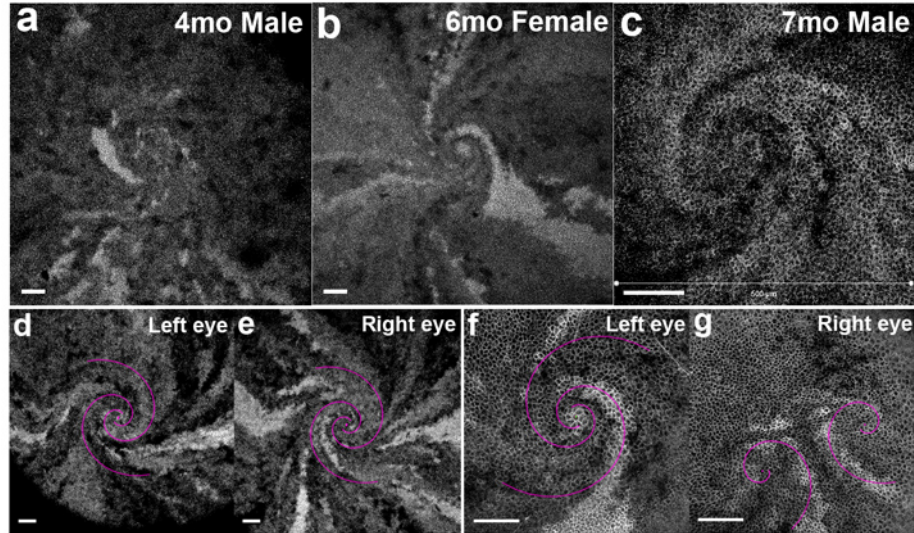


Fig2: Corneal patterns are sensitive to both genetic and environmental effects. Inter (a-c) and intra (d-g) individual comparisons to demonstrate sample range of possible behaviors. Although the series (a-c) is placed according to age, the most symmetric form is (b). Therefore, a linear description requires increased time resolution. Both similar (d,e) and dissimilar (f,g) forms are possible within individuals. All scale bars are  $100\mu\text{m}$  in this report. Images were captured only under two magnifications: size of “low-magnification” field is  $1240\mu\text{m}$  wide (a,b,d,e), while “high-magnification” is  $500\mu\text{m}$  wide (c,f,g).



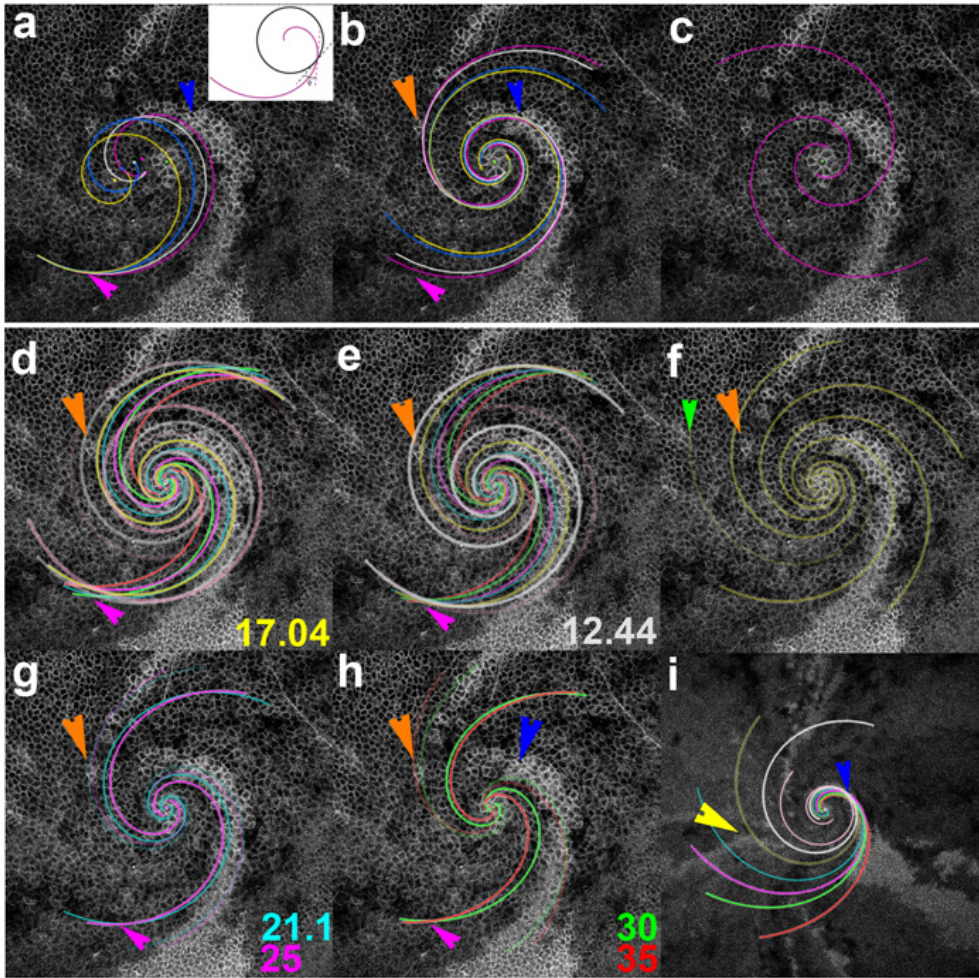


Fig3: Generating best fit through line fitting. (a-c) Rules of matching. Features (colored arrows) are selected and logarithmic forms with specific pitch angle are masked over features. Best match is produced through direct comparison after rotation and translation upon selection of two features. For example, closeness to a bright cluster of cells (orange arrow in b) is determined after selecting the pole (green dot) and edge (purple arrow) to root features. Flipping the symmetry demonstrates reasonable agreement that purple curves are matched better onto features in (b) than in (c). Curves in (a-c) represent a blinded trial. Once selected, purple curves ( $17^\circ$ ) were colored gold in (d-i), which contains a series ranging from  $8^\circ$  (pink) to  $35^\circ$  (red). To perform targeted search, the golden spiral is rotated in  $72^\circ$  increments in (f). (i) is a lower-magnification view of (a-h). Orientation is not exactly preserved in (i) compared to (a-h).

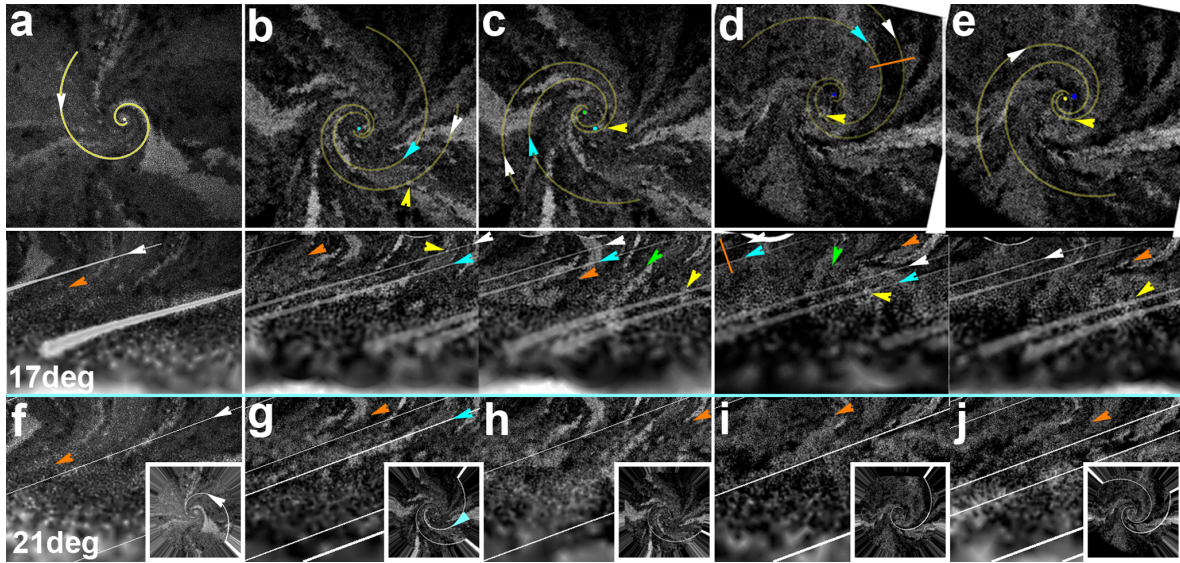


Fig4: Verification of  $\phi$  and M51 spirals as best fits. Three (a, b/c, d/e) independent corneas imaged using a 10X objective were directly matched to either a  $17^\circ$  (a-e) or  $21^\circ$  (f-j) spiral and examined for straight lines after log transformation. Corresponding white, teal arrows and orange bars are placed to assist reader orientation. Orange arrows represent our recognition of straight lines other than those marked by masked spirals. Green arrows mark straight lines that do not fit expected angles. Inset in (f-j) are back-transformed data.



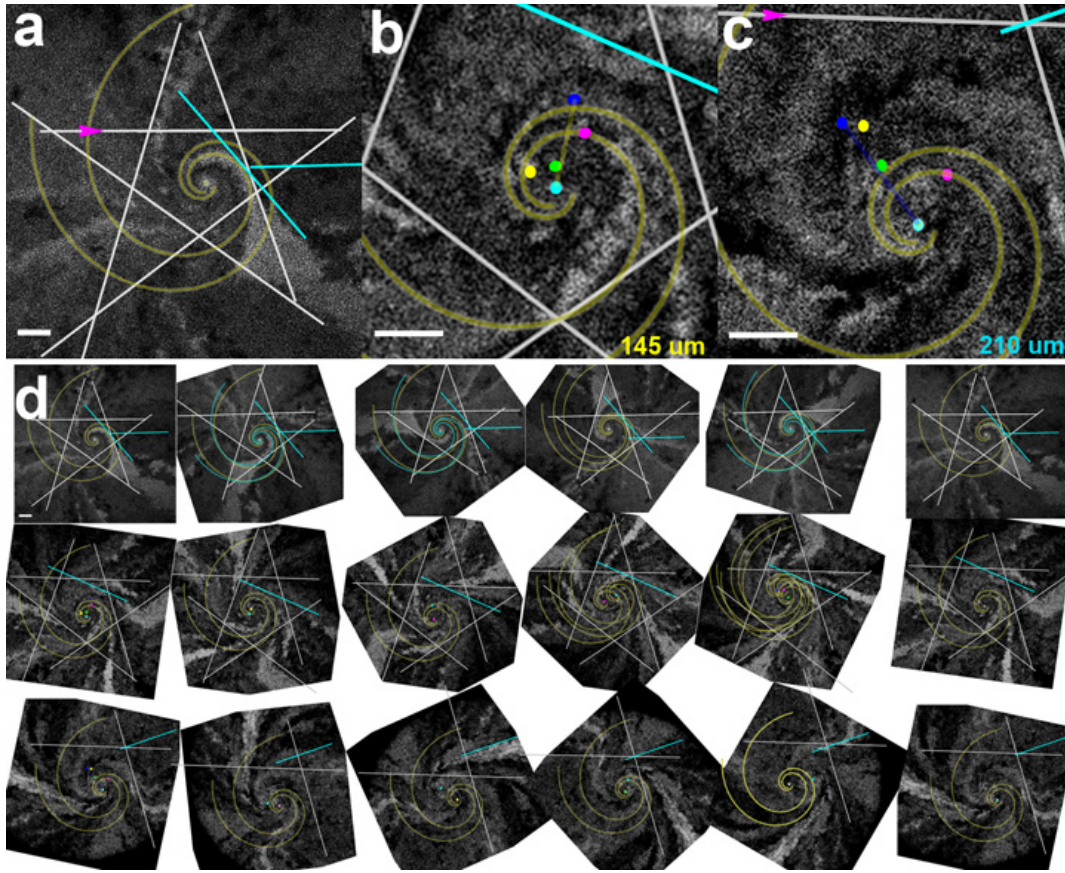


Fig5: Samples do not display same rotational symmetry. a) White lines are masked over recognized features. Teal lines mark lines that are preserved after  $72^\circ$  rotation. Exact position is not conserved. Using the top line of the pentagon (purple arrows, a,c), misoriented samples (b,c) were normalized, then scanned for features that match the chosen curves. The worksheet (d) is displayed to familiarize the reader to the process. Poles are landmarked as colored dots, collated, measured and represented (b,c). Size of core is measured as length of the most separated poles (teal and blue dots). Scale bars are  $100\mu\text{m}$ . Axial symmetry correlates with size of core, *i.e.*, the smaller the core, the greater the symmetry.

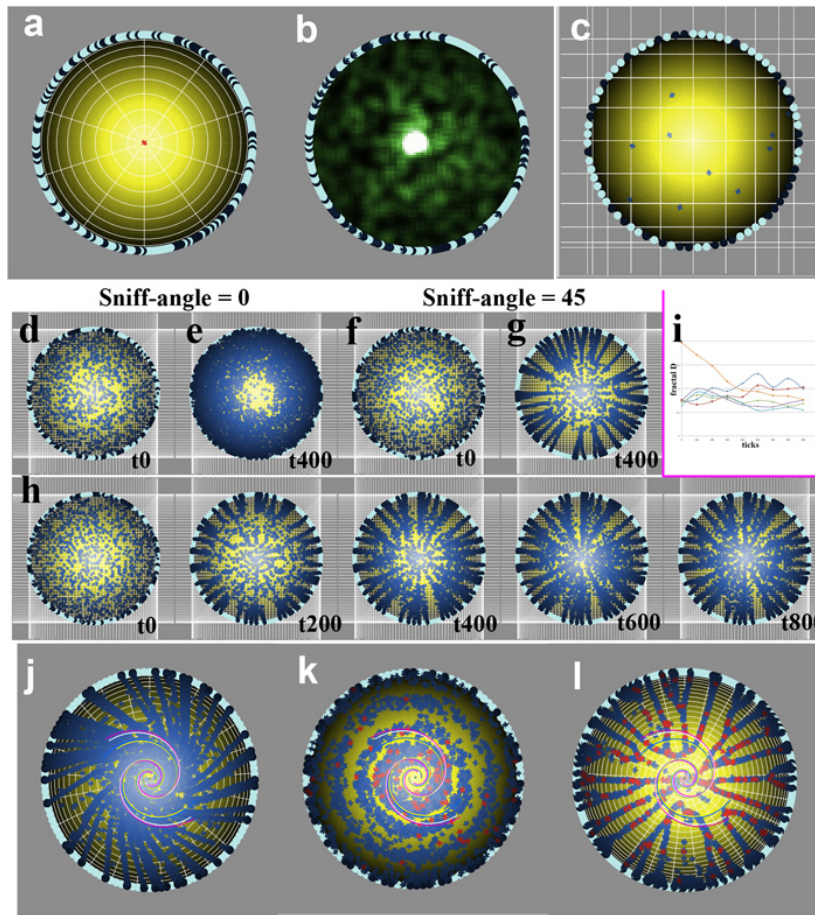


Fig6: Verification (a-c), deductions (d-h) and inductions (j-l) of Netlogo model. The surface of the stroma contains a bias (a, shade of yellow), with highest value at the apex (position of red maple leaf), to which patches of cells (agents, maple leaves) respond. Agents secrete a chemical (bright in green background) to which other agents respond. User controls movements by assigning a probability to heading with respect to the sensed values. Global arrangement of agents can be measured by box counting (c) and exporting to a spreadsheet to determine fractal dimension,  $D$  (i). (d,e;f,g) represent export views from two distinct simulations to illustrate pattern changes after manipulating agent's ability to detect local values (Sniff-angle=0 vs. 68). (h) Export views placed in series from a single simulation to illustrate qualitative shape changes, quantified in the associated graph (i). Graphing fractal dimension over time (ticks) allows assessment of global constraints (i). Outlier at  $t=0$  is due to doubling of initial number of agents. Distribution after 800 ticks demonstrates that final arrangement is independent of initial conditions. Quick comparisons using the  $\phi$  spiral (j-l) against deduced solutions demonstrate that the mechanism does not provide confidence as to whether the phenomenon is represented.

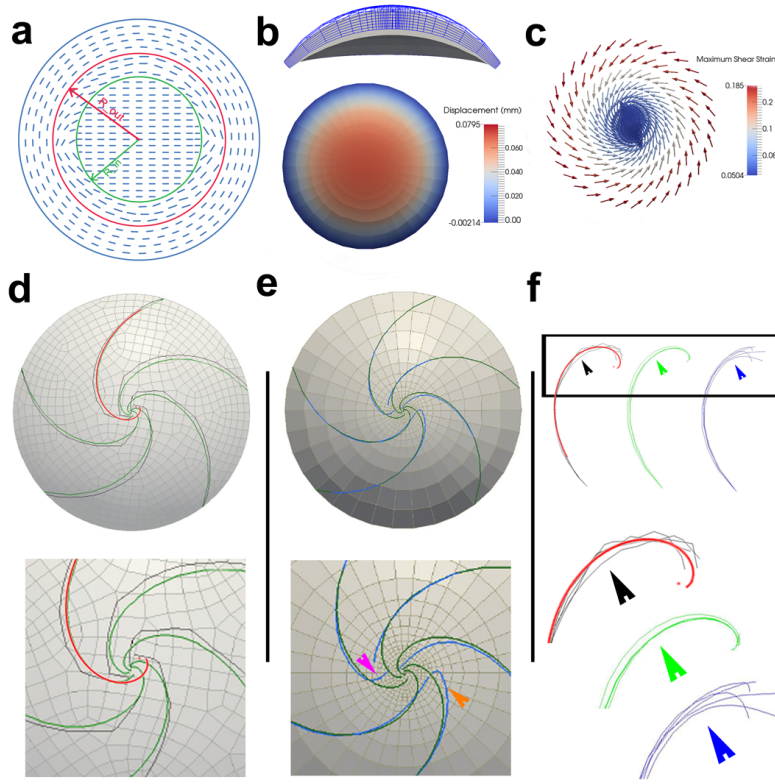


Fig7: FEM model produces  $35^\circ$  logarithmic curves that can be modified through manipulation of collagen arrangements. (a) An FEM model was produced based on approximate collagen orientations from published data. (b) Displacement under simulation of intraocular pressure is shown in cross-section in upper panel (wire frame is deformed mesh, solid is initial shape). Vertical displacement is colored by magnitude in bottom panel. (c) From the deformed shape, we produced a vector field of the maximum in-plane shear strain on the upper layer of the mesh. An algorithm with directional bias toward the center was used to compute individual pathlines by coupling local heading sampled at intersections of unstructured (background, d) or radially patterned meshes (background, f). Black curves in (d,f) represent solutions to unstructured mesh under isotropic conditions, green curves in (d-f) represent simulations under isotropic conditions on a radial mesh. Blue curves represent simulations under anisotropic conditions on a radial mesh. Purple and orange arrows in (e) point to curves that are greater than or lesser than  $35^\circ$  curves, respectively. Images along the bottom row in (d-f) are magnifications of the above. All black, green and blue arrows in (f) mark the same spot on collated curves. Red curves mark  $35^\circ$  logarithmic shapes.

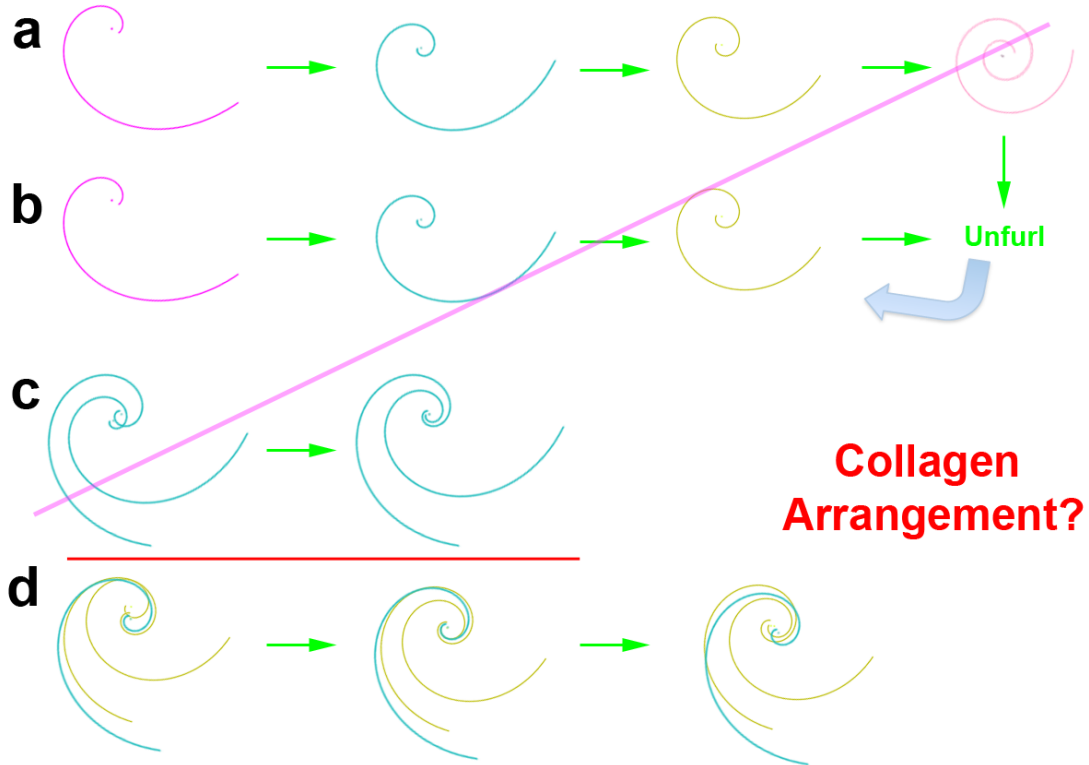


Fig8: We conclude that  $\phi$  (gold) and M51 (teal) spirals co-exist and are stable but poles are differently aligned (d). The purple line reflects rejected imaginations<sup>123</sup> of spiral sequence based on limited sampling. Arrows mark elapsed time. Different colored curves represent different pitch angles. “Collagen arrangement?” in red asks whether stromal organization is simultaneous with epithelial patterns, that is, whether collagen arrangements can be directly inferred from classification of basal epithelial patterns.

## References

1. Sharp, P. A.; Langer, R. Research agenda. Promoting convergence in biomedical science. *Science* 2011, 333, 527.
2. Weaver, W. Science and Complexity. *American Scientist* 1948, 36, 536-544.
3. Council, N. R. *A New Biology for the 21st Century*, 2009.
4. Alberts, B. M. How targeted should research and higher education be? *Acad Med* 1994, 69, 180-184.
5. Odum, E. P. The emergence of ecology as a new integrative discipline. *Science* 1977, 195, 1289-1293.
6. Powell, K. Stem-cell niches: it's the ecology, stupid! *Nature* 2005, 435, 268-270.
7. Schuster, P. Is There a Newton of the Blade of Grass? *Complexity* 2011, 16, 5-9.
8. Peirce, C. S. *Collected Papers of Charles Sanders Peirce*, 8 vols. Hartshorne, C.; Weiss, P.; Burks, A. W., Eds.; Harvard University Press.
9. AAAS. Project 2061. In Chpt 1: The Nature of Science; Chpt 12: Habits of Mind, 2009.
10. Simon, H. A.; Newell, A. Human Problem Solving: The State of the Theory in 1970. *American Psychologist* 1971, 26, 145-159.
11. Dewey, J. The American Association for the Advancement of Science: Science as Subject-Matter and as Method. *Science* 1910, 31, 121-127.
12. Dewey, J. Introduction. In *How We Think*, 1910.
13. Bruner, J. S. *The Process of Education*. Harvard University Press, 1999.
14. Ayala, F.; Adams, R. M.; Chilton, M.-D.; Holton, G.; Hull, D.; Patel, K.; Press, F.; Ruse, M.; Sharp, P. On being a scientist. *Proc Natl Acad Sci U S A* 1989, 86, 9053-9074.
15. Bodmer, W. F.; Artus, R. E.; Attenborough, D.; Blin-Stoyle, R. J.; Durham, K.; Mason, J.; Savory, M. J.; Swann, L.; Wedderburn, D.; Weston, M.; Ziman, J. M. The public understanding of science: report of the Royal Society's ad hoc group. The Royal Society 1985.
16. Gick, M. L.; Holyoak, K. J. Schema Induction and Analogical Transfer. *Cognitive Psychology* 1983, 15, 1-38.
17. Parnas, D. L.; Clements, P. C. A Rational Design Process: How and Why to Fake It. *IEEE Transactions on Software Engineering* 1986, SE-12, 251-257.
18. Okada, T.; Simon, H. A. Collaborative Discovery in a Scientific Domain. *Cognitive Science* 1997, 21, 109-146.
19. Barron, B. When Smart Groups Fail. *Journal of the Learning Sciences* 2003, 12, 307-359.
20. Salmon, W. C. Four decades of scientific explanation. University of Minnesota Press: Minneapolis, 1989, p 3-10.
21. Van Fraassen, B. C. The scientific image. In *Clarendon library of logic and philosophy*; Clarendon Press ; Oxford University Press: Oxford New York, 1980, p 141-146.



22. Boersema, D. Peirce on Explanation. *The Journal of Speculative Philosophy* 2003, 17, 224-236.
23. Frankfurt, H. G. Peirce's Notion of Abduction. *Journal of Philosophy* 1958, 55, 593-597.
24. Goebel, R. Abduction and its relation to constrained induction. *Proc. IJCAI '97 Workshop on Abduction and Induction in AI* 1997, 17-18.
25. Johnson-Laird, P. N. Mental models and human reasoning. *Proc Natl Acad Sci U S A* 2010, 107, 18243-18250.
26. Aldridge, A. E. Brachiopod outline and the importance of the logarithmic spiral. *Paleobiology* 1998, 24, 215-226.
27. McGhee Jr., G. R. The question of spiral axes and brachiopod shell growth: a comparison of morphometric techniques. *Paleobiology* 2001, 27, 716-723.
28. Cook, T. A. *The Curves of Life*. Dover Publications, Inc., New York, 1979.
29. Dunlap, R. A. *The Golden Ratio and Fibonacci Numbers*. World Scientific Publishing Co. Pte. Ltd., 1997.
30. Vanag, V. K.; Epstein, I. R. From the Cover: Segmented spiral waves in a reaction-diffusion system. *Proc Natl Acad Sci U S A* 2003, 100, 14635-14638.
31. Dormann, D.; Kim, J. Y.; Devreotes, P. N.; Weijer, C. J. cAMP receptor affinity controls wave dynamics, geometry and morphogenesis in *Dictyostelium*. *J Cell Sci* 2001, 114, 2513-2523.
32. Douady, S.; Couder, Y. Phyllotaxis as a Dynamical Self Organizing Process Part I: The Spiral Modes Resulting from Time-Periodic Iterations. *Journal of Theoretical Biology* 1995, 178, 255-274.
33. Devreotes, P. *Dictyostelium discoideum*: a model system for cell-cell interactions in development. *Science* 1989, 245, 1054-1058.
34. Adler, I. The Role of Mathematics in Phyllotaxis. In *Solving the Riddle of Phyllotaxis: Why the Fibonacci Numbers and the Golden Ratio Occur on Plants*; World Scientific Publishing Co. Pte. Ltd., 1998, p 171-174.
35. Gentner, D.; Rattermann, M. J.; Forbus, K. D. The Roles of Similarity in Transfer: Separating Retrievability from Inferential Soundness. *Cognitive Psychology* 1993, 25, 524-575.
36. Ruberti, J. W.; Zieske, J. D. Prelude to corneal tissue engineering - gaining control of collagen organization. *Prog Retin Eye Res* 2008, 27, 549-577.
37. Giraud Guille, M. M.; Nassif, N. N.; Fernandes, F. M. Collagen-based Materials for Tissue Repair, from Bio-inspired to Biomimetic. In *Materials Design Inspired by Nature: Function through Inner Architecture*. Fratzl, P.; Dunlop, J. W. C.; Weinkamer, R., Eds.; Royal Society of Chemistry, 2013, p 107-127.
38. Collinson, J. M.; Chanas, S. A.; Hill, R. E.; West, J. D. Corneal development, limbal stem cell function, and corneal epithelial cell migration in the Pax6(+/-) mouse. *Invest Ophthalmol Vis Sci* 2004, 45, 1101-1108.
39. Vithana, E. N.; Aung, T.; Khor, C. C.; Cornes, B. K.; Tay, W. T.; Sim, X.; Lavanya, R.; Wu, R.; Zheng, Y.; Hibberd, M. L.; Chia, K. S.; Seielstad, M.; Goh, L. K.; Saw, S. M.; Tai, E. S.; Wong, T. Y. Collagen-related genes influence the glaucoma risk factor, central corneal thickness. *Hum Mol Genet* 2011, 20, 649-658.
40. Sun, M.; Chen, S.; Adams, S. M.; Florer, J. B.; Liu, H.; Kao, W. W.; Wenstrup, R. J.; Birk, D. E. Collagen V is a dominant regulator of collagen fibrillogenesis:



dysfunctional regulation of structure and function in a corneal-stroma-specific Col5a1-null mouse model. *J Cell Sci* 2011, 124, 4096-4105.

41. Seo, S.; Singh, H. P.; Lacal, P. M.; Sasman, A.; Fatima, A.; Liu, T.; Schultz, K. M.; Losordo, D. W.; Lehmann, O. J.; Kume, T. Forkhead box transcription factor FoxC1 preserves corneal transparency by regulating vascular growth. *Proc Natl Acad Sci U S A* 2011, 109, 2015-2020.

42. Hillier, B. Spatial sustainability in cities: organic patterns and sustainable forms. *Proceedings of the 7th International Space Syntax Symposium* 2009, 1-20.

43. Bettencourt, L. M. The origins of scaling in cities. *Science* 2013, 340, 1438-1441.

44. Dua, H. S.; Watson, N. J.; Mathur, R. M.; Forrester, J. V. Corneal epithelial cell migration in humans: 'hurricane and blizzard keratopathy'. *Eye (Lond)* 1993, 7 ( Pt 1), 53-58.

45. Patel, D. V.; McGhee, C. N. In vivo laser scanning confocal microscopy confirms that the human corneal sub-basal nerve plexus is a highly dynamic structure. *Invest Ophthalmol Vis Sci* 2008, 49, 3409-3412.

46. Dua, H. S.; Singh, A.; Gomes, J. A.; Laibson, P. R.; Donoso, L. A.; Tyagi, S. Vortex or whorl formation of cultured human corneal epithelial cells induced by magnetic fields. *Eye (Lond)* 1996, 10 ( Pt 4), 447-450.

47. Collinson, J. M.; Morris, L.; Reid, A. I.; Ramaesh, T.; Keighren, M. A.; Flockhart, J. H.; Hill, R. E.; Tan, S. S.; Ramaesh, K.; Dhillon, B.; West, J. D. Clonal analysis of patterns of growth, stem cell activity, and cell movement during the development and maintenance of the murine corneal epithelium. *Dev Dyn* 2002, 224, 432-440.

48. Iannaccone, S.; Zhou, Y.; Walterhouse, D.; Taborn, G.; Landini, G.; Iannaccone, P. Three dimensional visualization and fractal analysis of mosaic patches in rat chimeras: cell assortment in liver, adrenal cortex and cornea. *PLoS One* 2012, 7, e31609.

49. Yu, C. Q.; Rosenblatt, M. I. Transgenic corneal neurofluorescence in mice: a new model for in vivo investigation of nerve structure and regeneration. *Invest Ophthalmol Vis Sci* 2007, 48, 1535-1542.

50. Leiper, L. J.; Ou, J.; Walczysko, P.; Kucerova, R.; Lavery, D. N.; West, J. D.; Collinson, J. M. Control of patterns of corneal innervation by Pax6. *Invest Ophthalmol Vis Sci* 2009, 50, 1122-1128.

51. Wang, C.; Fu, T.; Xia, C.; Li, Z. Changes in mouse corneal epithelial innervation with age. *Invest Ophthalmol Vis Sci* 2012, 53, 5077-5084.

52. Erie, J. C.; McLaren, J. W.; Hodge, D. O.; Bourne, W. M. The effect of age on the corneal subbasal nerve plexus. *Cornea* 2005, 24, 705-709.

53. Mort, R. L.; Ramaesh, T.; Kleinjan, D. A.; Morley, S. D.; West, J. D. Mosaic analysis of stem cell function and wound healing in the mouse corneal epithelium. *BMC Dev Biol* 2009, 9, 4.

54. Nagasaki, T.; Zhao, J. Centripetal movement of corneal epithelial cells in the normal adult mouse. *Invest Ophthalmol Vis Sci* 2003, 44, 558-566.

55. Patel, D. V.; McGhee, C. N. Mapping of the normal human corneal sub-Basal nerve plexus by in vivo laser scanning confocal microscopy. *Invest Ophthalmol Vis Sci* 2005, 46, 4485-4488.

56. McCaig, C. D.; Rajnicek, A. M.; Song, B.; Zhao, M. Controlling cell behavior electrically: current views and future potential. *Physiol Rev* 2005, 85, 943-978.
57. Lemp, M. A.; Mathers, W. D. Corneal epithelial cell movement in humans. *Eye (Lond)* 1989, 3 ( Pt 4), 438-445.
58. Majo, F.; Rochat, A.; Nicolas, M.; Jaoude, G. A.; Barrandon, Y. Oligopotent stem cells are distributed throughout the mammalian ocular surface. *Nature* 2008, 456, 250-254.
59. Mort, R. L.; Douvaras, P.; Morley, S. D.; Dora, N.; Hill, R. E.; Collinson, J. M.; West, J. D. Stem cells and corneal epithelial maintenance: insights from the mouse and other animal models. *Results Probl Cell Differ* 2012, 55, 357-394.
60. Getsios, S.; Huen, A. C.; Green, K. J. Working out the strength and flexibility of desmosomes. *Nat Rev Mol Cell Biol* 2004, 5, 271-281.
61. Mukhopadhyay, M.; Gorivodsky, M.; Shtrom, S.; Grinberg, A.; Niehrs, C.; Morasso, M. I.; Westphal, H. Dkk2 plays an essential role in the corneal fate of the ocular surface epithelium. *Development* 2006, 133, 2149-2154.
62. Suzuki, K.; Saito, J.; Yanai, R.; Yamada, N.; Chikama, T.; Seki, K.; Nishida, T. Cell-matrix and cell-cell interactions during corneal epithelial wound healing. *Prog Retin Eye Res* 2003, 22, 113-133.
63. Zheng, D.; Giljohann, D. A.; Chen, D. L.; Massich, M. D.; Wang, X. Q.; Iordanov, H.; Mirkin, C. A.; Paller, A. S. Topical delivery of siRNA-based spherical nucleic acid nanoparticle conjugates for gene regulation. *Proc Natl Acad Sci U S A* 2012, 109, 11975-11980.
64. Aida, T.; Meijer, E. W.; Stupp, S. I. Functional supramolecular polymers. *Science* 2012, 335, 813-817.
65. Ghatge, D.; Edelhauser, H. F. Barriers to glaucoma drug delivery. *J Glaucoma* 2008, 17, 147-156.
66. Pajoohesh-Ganji, A.; Pal-Ghosh, S.; Simmens, S. J.; Stepp, M. A. Integrins in slow-cycling corneal epithelial cells at the limbus in the mouse. *Stem Cells* 2006, 24, 1075-1086.
67. Jester, J. V.; Huang, J.; Petroll, W. M.; Cavanagh, H. D. TGFbeta induced myofibroblast differentiation of rabbit keratocytes requires synergistic TGFbeta, PDGF and integrin signaling. *Exp Eye Res* 2002, 75, 645-657.
68. Katchalsky, A. Thermodynamics of Flow and Biological Organization. *Zygon: Journal of Religion and Science* 1971, 6, 99-125.
69. Bonanno, J. A. Molecular mechanisms underlying the corneal endothelial pump. *Exp Eye Res* 2012, 95, 2-7.
70. Cheng, X.; Pinsky, P. M. Mechanisms of self-organization for the collagen fibril lattice in the human cornea. *J R Soc Interface* 2013, 10, 20130512.
71. Cotsarelis, G.; Cheng, S. Z.; Dong, G.; Sun, T. T.; Lavker, R. M. Existence of slow-cycling limbal epithelial basal cells that can be preferentially stimulated to proliferate: implications on epithelial stem cells. *Cell* 1989, 57, 201-209.
72. Muzumdar, M. D.; Tasic, B.; Miyamichi, K.; Li, L.; Luo, L. A global double-fluorescent Cre reporter mouse. *Genesis* 2007, 45, 593-605.
73. Rhee, J. M.; Pirity, M. K.; Lackan, C. S.; Long, J. Z.; Kondoh, G.; Takeda, J.; Hadjantonakis, A. K. In vivo imaging and differential localization of lipid-modified GFP-variant fusions in embryonic stem cells and mice. *Genesis* 2006, 44, 202-218.

74. Hayashi, Y.; Call, M. K.; Liu, C. Y.; Hayashi, M.; Babcock, G.; Ohashi, Y.; Kao, W. W. Monoallelic expression of Krt12 gene during corneal-type epithelium differentiation of limbal stem cells. *Invest Ophthalmol Vis Sci* 2010, 51, 4562-4568.
75. Jahner, D.; Stuhlmann, H.; Stewart, C. L.; Harbers, K.; Lohler, J.; Simon, I.; Jaenisch, R. De novo methylation and expression of retroviral genomes during mouse embryogenesis. *Nature* 1982, 298, 623-628.
76. Goll, M. G.; Anderson, R.; Stainier, D. Y.; Spradling, A. C.; Halpern, M. E. Transcriptional silencing and reactivation in transgenic zebrafish. *Genetics* 2009, 182, 747-755.
77. Llopis, J.; McCaffery, J. M.; Miyawaki, A.; Farquhar, M. G.; Tsien, R. Y. Measurement of cytosolic, mitochondrial, and Golgi pH in single living cells with green fluorescent proteins. *Proc Natl Acad Sci U S A* 1998, 95, 6803-6808.
78. Nijhout, H. F. Development and evolution of adaptive polyphenisms. *Evol Dev* 2003, 5, 9-18.
79. Sorrenti, A.; Illa, O.; Ortuno, R. M. Amphiphiles in aqueous solution: well beyond a soap bubble. *Chem Soc Rev* 2013, 42, 8200-8219.
80. Tsotsos, J. K. Knowledge and the Visual Process: Content, Form and Use. *Pattern Recognition* 1984, 17, 13-27.
81. Falbo, C. The Golden Ratio—A Contrary Viewpoint. *The College Mathematics Journal* 2005, 36, 123-134.
82. Shipman, P. D.; Sun, Z.; Pennybacker, M.; Newell, A. C. How universal are Fibonacci patterns? *The European Physical Journal D* 2011, 62, 5-17.
83. Shetty, R.; Vogel, S. N.; Ostriker, E. C.; Teuben, P. J. Kinematics of Spiral-arm Streaming in M51. *The Astrophysics Journal* 2007, 665, 1138-1158.
84. Patel, D. V.; McGhee, C. N. Mapping the corneal sub-basal nerve plexus in keratoconus by in vivo laser scanning confocal microscopy. *Invest Ophthalmol Vis Sci* 2006, 47, 1348-1351.
85. Raup, D. M. Goemetric Analysis of Shell Coiling: General Problems. *Journal of Paleontology* 1966, 40, 1178-1190.
86. Kahneman, D. A Perspective on Judgment and Choice. *American Psychologist* 2003, 9, 697-720.
87. Dewey, J. Logic of Judgments of Practice. In *Essays in Experimental Logic*; University of Chicago Press, 2004, p 241.
88. Treisman, A. Perceiving and re-perceiving objects. *Am Psychol* 1992, 47, 862-875.
89. Wilensky, U.; Reisman, K. Thinking Like a Wolf, a Sheep, or a Firefly: Learning Biology Through Constructing and Testing Computational Theories—An Embodied Modeling Approach. *COGNITION AND INSTRUCTION* 2006, 24, 171-209.
90. Sheppard, J.; Hayes, S.; Boote, C.; Votruba, M.; Meek, K. M. Changes in corneal collagen architecture during mouse postnatal development. *Invest Ophthalmol Vis Sci* 2010, 51, 2936-2942.
91. Gautieri, A.; Vesentini, S.; Redaelli, A.; Buehler, M. J. Hierarchical structure and nanomechanics of collagen microfibrils from the atomistic scale up. *Nano Lett* 2011, 11, 757-766.
92. Simon, H. A. The Structure of Ill Structured Problems. *Artificial Intelligence* 1973, 4, 181-201.

93. Newell, A. C.; Shipman, P. D.; Sun, Z. Phyllotaxis: cooperation and competition between mechanical and biochemical processes. *J Theor Biol* 2008, 251, 421-439.
94. Fratzl, P.; Weinkamer, R. Nature's hierarchical materials. *Progress in Materials Science* 2007, 52, 1263-1334.
95. Saeidi, N.; Karmelek, K. P.; Paten, J. A.; Zareian, R.; DiMasi, E.; Ruberti, J. W. Molecular crowding of collagen: a pathway to produce highly-organized collagenous structures. *Biomaterials* 2012, 33, 7366-7374.
96. Reznikov, N.; Shahar, R.; Weiner, S. Three-dimensional structure of human lamellar bone: the presence of two different materials and new insights into the hierarchical organization. *Bone* 2013, 59, 93-104.
97. Chamberlin, T. C. The Method of Multiple Working Hypotheses: With this method the dangers of parental affection for a favorite theory can be circumvented. *Science* 1965, 148, 754-759.
98. Jean, R. V. Growth and Entropy: Phylogenism in Phyllotaxis. *Journal of Theoretical Biology* 1978, 71, 639-660.
99. Harman, G. H. The Inference to the Best Explanation. *The Philosophical Review* 1965, 74, 88-95.
100. Holmes, D. F.; Kadler, K. E. The precision of lateral size control in the assembly of corneal collagen fibrils. *J Mol Biol* 2005, 345, 773-784.
101. Boote, C.; Dennis, S.; Newton, R. H.; Puri, H.; Meek, K. M. Collagen fibrils appear more closely packed in the prepupillary cornea: optical and biomechanical implications. *Invest Ophthalmol Vis Sci* 2003, 44, 2941-2948.
102. Morishige, N.; Nishida, T.; Jester, J. V. Second harmonic Generation for Visualizing 3-Dimensional Structure of Corneal Collagen Lamellae. *Cornea* 2009, 28, S46-S53.
103. Winkler, M.; Chai, D.; Kriling, S.; Nien, C. J.; Brown, D. J.; Jester, B.; Juhasz, T.; Jester, J. V. Nonlinear optical macroscopic assessment of 3-D corneal collagen organization and axial biomechanics. *Invest Ophthalmol Vis Sci* 2011, 52, 8818-8827.
104. Chakravarti, S.; Petroll, W. M.; Hassell, J. R.; Jester, J. V.; Lass, J. H.; Paul, J.; Birk, D. E. Corneal opacity in lumican-null mice: defects in collagen fibril structure and packing in the posterior stroma. *Invest Ophthalmol Vis Sci* 2000, 41, 3365-3373.
105. Wang, L.; Uhlig, P. C.; Eikenberry, E. F.; Robenek, H.; Bruckner, P.; Hansen, U. Lateral growth limitation of corneal fibrils and their lamellar stacking depend on covalent collagen cross-linking by transglutaminase-2 and lysyl oxidases, respectively. *J Biol Chem* 2013, 289, 921-929.
106. Martin, R.; Farjanel, J.; Eichenberger, D.; Colige, A.; Kessler, E.; Hulmes, D. J.; Giraud-Guille, M. M. Liquid crystalline ordering of procollagen as a determinant of three-dimensional extracellular matrix architecture. *J Mol Biol* 2000, 301, 11-17.
107. Bill, A. Blood circulation and fluid dynamics in the eye. *Physiol Rev* 1975, 55, 383-417.
108. Reitsamer, H. A.; Kiel, J. W. A rabbit model to study orbital venous pressure, intraocular pressure, and ocular hemodynamics simultaneously. *Invest Ophthalmol Vis Sci* 2002, 43, 3728-3734.

109. Heier, C. R.; Hampton, T. G.; Wang, D.; Didonato, C. J. Development of electrocardiogram intervals during growth of FVB/N neonate mice. *BMC Physiol* 2010, 10, 16.
110. Jaeger, H. M.; Miskin, M. Z.; Waitukaitis, S. R. From Nanoscale Cohesion To Macroscale Entanglement: Opportunities For Designing Granular Aggregate Behavior By Tailoring Grain Shape And Interactions. *Powders & Grains 2013, AIP Conf. Proc.* 2013, 1542, 3-6.
111. Waddington, C. H. Form, End and Time. In *The Strategy of the Genes: A Discussion of Some Aspects of Theoretical Biology*; George Allen & Unwin Ltd.: London, 1957, p 1-10.
112. Hulmes, D. J.; Wess, T. J.; Prockop, D. J.; Fratzl, P. Radial packing, order, and disorder in collagen fibrils. *Biophys J* 1995, 68, 1661-1670.
113. Levin, S. A. The Problem of Pattern and Scale in Ecology. *Ecology* 1992, 73, 1943-1967.
114. Liu, X.; Wu, H.; Byrne, M.; Jeffrey, J.; Krane, S.; Jaenisch, R. A targeted mutation at the known collagenase cleavage site in mouse type I collagen impairs tissue remodeling. *J Cell Biol* 1995, 130, 227-237.
115. Church, A. H. On the Relation of Phyllotaxis to Mechanical Laws. *Williams and Norgate*, 1904.
116. Charvolin, J.; Sadoc, J.-F. A Phyllotactic Approach to the Structure of Collagen Fibrils. *Biophysical Reviews and Letters* 2011, 6, 1-15.
117. Reznikov, N.; Shahar, R.; Weiner, S. Three-dimensional structure of human lamellar bone: the presence of two different materials and new insights into the hierarchical organization. *Bone* 2014, 59, 93-104.
118. Meek, K. M.; Boote, C. The use of X-ray scattering techniques to quantify the orientation and distribution of collagen in the corneal stroma. *Prog Retin Eye Res* 2009, 28, 369-392.
119. Lipton, P. *Inference to the Best Explanation*. Routledge Taylor and Francis Group, 2004.
120. Ottino, J. M. Is a picture worth 1,000 words? *Nature* 2003, 421, 474-476.
121. Foster, C. D.; Mohammad Nejad, T. Trilinear Hexahedra with Integral-Averaged Volumes for Nearly Incompressible Nonlinear Deformation. *Computers and Structures* 2013, Submitted.
122. Foster, C. D.; Borja, R. I.; Regueiro, R. A. Modeling the effects of variable friction in fractured geomaterials in an embedded strong discontinuity finite element setting. *International Journal for Numerical Methods in Engineering* 2007, 72, 549-581.
123. Dewey, J. Activity and the Training of Thought; Some General Conclusions. In *How We Think*, 1933, p 166, 223-224.